

Bandgap Engineering of Two-Step Processed Perovskite Top Cells for Perovskite-Based Tandem Photovoltaics

Ronja Pappenberger, Alexander Diercks, Julian Petry, Somayeh Moghadamzadeh, Paul Fassel, and Ulrich W. Paetzold*

For high-performance application of perovskite solar cells (PSCs) in monolithic perovskite/silicon tandem configuration, an optimal bandgap and process method of the perovskite top cell is required. While the two-step method leads to regular perovskite film crystallization, engineering wider bandgaps ($E_g > 1.65$ eV) for the solution-based two-step method remains a challenge. This work introduces an effective and facile strategy to increase the bandgap of two-step solution-processed perovskite films by incorporating bromide in both deposition steps, the inorganic precursor deposition (step 1, PbBr_2) and the organic precursor deposition (step 2, FABr). This strategy yields improved charge carrier extraction and quasi-Fermi level splitting with power conversion efficiencies (PCEs) of up to 15.9%. Further improvements are achieved by introducing CsI in the bulk and utilizing LiF as surface passivation, resulting in a stable power output exceeding 18.5% for $E_g = 1.68$ eV. This additional performance boost arises from enhanced perovskite film crystallization, leading to improved charge carrier extraction. Laboratory scale monolithic perovskite/silicon solar cells (TSCs) (1 cm^2 active area) achieve PCEs up to 23.7%. This work marks a significant advancement for wide bandgap two-step solution-processed perovskite films, enabling their effective use in high-performance and reproducible PSCs and perovskite/silicon TSCs.

around 29%,^[1] power conversion efficiencies (PCEs) of up to 33.7%^[2] have been recently demonstrated for monolithic perovskite/silicon tandem solar cells (TSCs). Hybrid lead halide perovskite solar cells (PSCs) are the perfect partner for silicon bottom solar cells, given favorable optoelectronic properties and a tunable bandgap in a wide spectral range (1.5 to 2.3 eV).^[3–5]

Currently, the vast majority of high efficiency perovskite/silicon TSCs are fabricated using one-step deposition processes with antisolvent quenching.^[6–10] Although the one-step method is simpler to operate even on a laboratory scale, the surface coverage and uniformity of the resulting film are a major concern as the thin film crystallization is hard to control.^[11–13] Consequently, processing dense perovskite thin films using the one-step method is very demanding.^[14] One of the most promising routes to process uniform and high-quality perovskite thin films (thickness $< 1 \mu\text{m}$) is the two-step method.^[15,16] This route, comprising the subsequent deposition of the Pb-containing precursor

materials and the organic cations, was first introduced by Mitzi et al.^[17] in 1998 and further developed for PSC application by Grätzel et al.^[18,19] from 2013 onwards. Due to the top-down penetration of the organic precursors in the second step, the two-step method facilitates the conformal coating of dense and pinhole-free perovskite thin films on silicon bottom solar cells, leading to higher achievable PCEs.^[15,16] In addition, greater flexibility in perovskite composition, employed solvents and the capability to process over larger areas using deposition techniques such as evaporation are key advantages of the two-step method.^[13–15] However, so far, the solution-based two-step method was almost exclusively used for PSCs with a narrow bandgap (< 1.60 eV),^[20–22] while optical simulations show that in monolithic tandem configuration wider bandgaps (> 1.65 eV) are required for an optimal performance.^[6,23–28] By changing the bromide/iodide ratio in a perovskite composition ($\text{X} = \text{I}_{1-\gamma}\text{Br}_\gamma$, $0 \leq \gamma \leq 1$), the bandgap of the perovskite is tunable.^[29,30] While the hybrid two-step method has been successfully used to produce wide bandgap PSCs for tandem applications by incorporating CsBr ,^[31–34] the incorporation of bromide in the solution-based two-step method remains a more intricate endeavor.

1. Introduction

While market-dominating single-junction silicon photovoltaics (PVs) are approaching their theoretical efficiency limit of

R. Pappenberger, J. Petry, S. Moghadamzadeh, P. Fassel, U. W. Paetzold
Institute of Microstructure Technology (IMT)
Karlsruhe Institute of Technology (KIT)
Hermann-von-Helmholtz-Platz 1, 76344 Eggenstein-Leopoldshafen,
Germany
E-mail: ulrich.paetzold@kit.edu

R. Pappenberger, A. Diercks, J. Petry, S. Moghadamzadeh, P. Fassel,
U. W. Paetzold
Light Technology Institute (LTI)
Karlsruhe Institute of Technology (KIT)
Engesserstrasse 13, 76131 Karlsruhe, Germany

The ORCID identification number(s) for the author(s) of this article can be found under <https://doi.org/10.1002/adfm.202311424>

© 2023 The Authors. Advanced Functional Materials published by Wiley-VCH GmbH. This is an open access article under the terms of the Creative Commons Attribution-NonCommercial License, which permits use, distribution and reproduction in any medium, provided the original work is properly cited and is not used for commercial purposes.

DOI: 10.1002/adfm.202311424

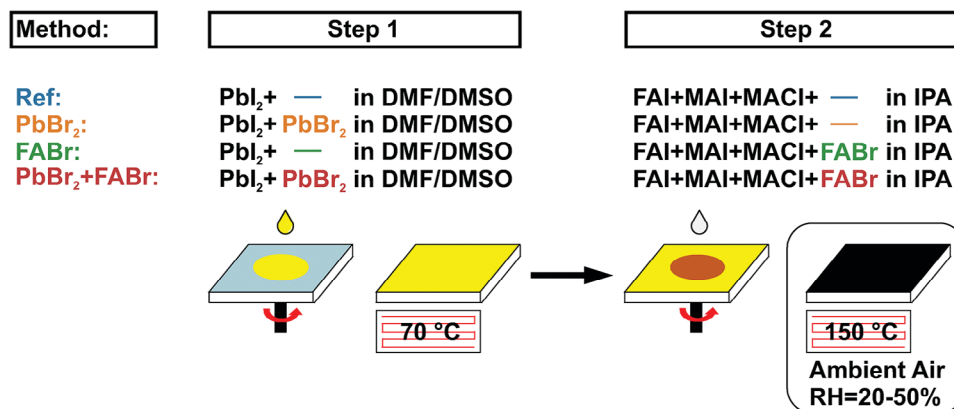


Figure 1. Schematic illustration of the employed solution-based two-step deposition method for fabrication of the reference perovskite films (labeled as Ref) and the perovskite films with higher bromide content. The bromide is either incorporated via PbBr₂ in the first deposition step, via FABr in the second deposition step or via a combination of PbBr₂ and FABr in the first and second deposition step (labeled as PbBr₂, FABr, and PbBr₂+FABr, respectively).

Two primary strategies exist for incorporating bromide within the two-step method: First, bromide can be incorporated via lead bromide (PbBr₂) into the inorganic precursor (lead iodide, PbI₂) solution during the first deposition step. Second, bromide can be incorporated during the second deposition step, encompassing the deposition of organic precursors such as formammonium bromide (FABr) or methylammonium bromide (MABr). Each strategy has inherent constraints.^[15,16] The incorporation of bromide in the first deposition step leads to a PbBr₂ film with a bulk structure that impedes interdiffusion of organic cations during the second step, causing incomplete conversion and residual PbI₂.^[16,35,36] Consequently, excessive PbI₂ residuals can induce pronounced hysteresis and diminished stability in the resultant perovskite film.^[37] Additionally, the presence of undercoordinated Pb ions, serving as non-radiative recombination sites, can result in charge carrier recombination and ionic motion, which in turn limits the overall performance of the device.^[38–43] This effect holds particular significance for solar cells in a *p-i-n* configuration, where the remaining PbI₂ layer can hinder the effective extraction of charges to the underlying transport layer, possibly resulting in the formation of a counter diode.^[44] Incorporation of bromide during the second deposition step poses a challenge with regard to bromide diffusion into the lead halide layer, which arises from the elevated activation energy needed for the migration of bromide anions in comparison to iodide anions.^[45–47] This increased energetic barrier hinders the formation of the final perovskite material, affecting overall performance. Consequently, the question arises as to how the optimal amount of bromide can be effectively controlled and incorporated into the inorganic/organic precursor solution in order to obtain high-quality PSCs with a wider bandgap.

This work introduces an effective and facile way to incorporate bromide into the two-step processed perovskite thin films, thereby increasing the bandgap of the perovskite beyond 1.65 eV. The proposed strategy involves a combined incorporation of PbBr₂ (first deposition step, added in the inorganic solution) and FABr (second deposition step, added in the organic cation solution). This combination improves the bromide incorporation and

enhances the bulk properties of the perovskite layer. Utilizing this strategy and adding CsI in the bulk and using LiF as surface passivation, *p-i-n* type wide bandgap ($E_g = 1.68$ eV) PSCs and their corresponding perovskite/silicon TSCs with high performance and suppressed hysteresis are achieved with the solution-based two-step deposition method. Combined bromide incorporation in both deposition steps via PbBr₂ and FABr with CsI in the bulk and LiF as surface passivation facilitates effective interdiffusion of organic materials, resulting in efficiencies of 18.5% for small-area (active area of 7.84 mm²) single-junction PSCs and up to 23.7% for monolithic TSCs (active area of 1 cm²).

2. Results and Discussion

The two-step method employed for fabricating the perovskite thin films in this work is illustrated in **Figure 1**, which is based on an established recipe as introduced by Gutierrez-Partida et al.^[48] (labeled as Ref). The reference perovskite's structural formula is MA_{0.07}FA_{0.93}PbI₃ with a bandgap of ≈ 1.55 eV (Figure S9a, Supporting Information). For reference PSCs a champion PCE of 19.38% and 18.91% in the backward and forward scan is achieved, respectively (Table S1, Supporting Information). The device architecture of the PSCs consists of the layer stack ITO/NiO_x/2PACz/perovskite/C₆₀/BCP/Ag with an active area of 7.84 mm² and is presented in **Figure 2a**.

To investigate the bromide incorporation in the perovskite thin film, three distinct strategies are benchmarked: 1. Bromide is added in the first deposition step, replacing some parts of PbI₂ by PbBr₂ (labeled as PbBr₂), 2. Bromide is added in the second deposition step, replacing some parts of FAI by FABr (labeled as FABr) or 3. Bromide is added by a combination of PbBr₂ and FABr (labeled as PbBr₂+FABr) in the first and second deposition step. It should be highlighted that – in contrast to other reports^[15,16] – no further additives apart of methylammonium chloride (MACl) are employed.

To ensure a meaningful comparison among all strategies explored to incorporate bromide, the bandgap of all processed perovskite thin films is determined based on the differential of

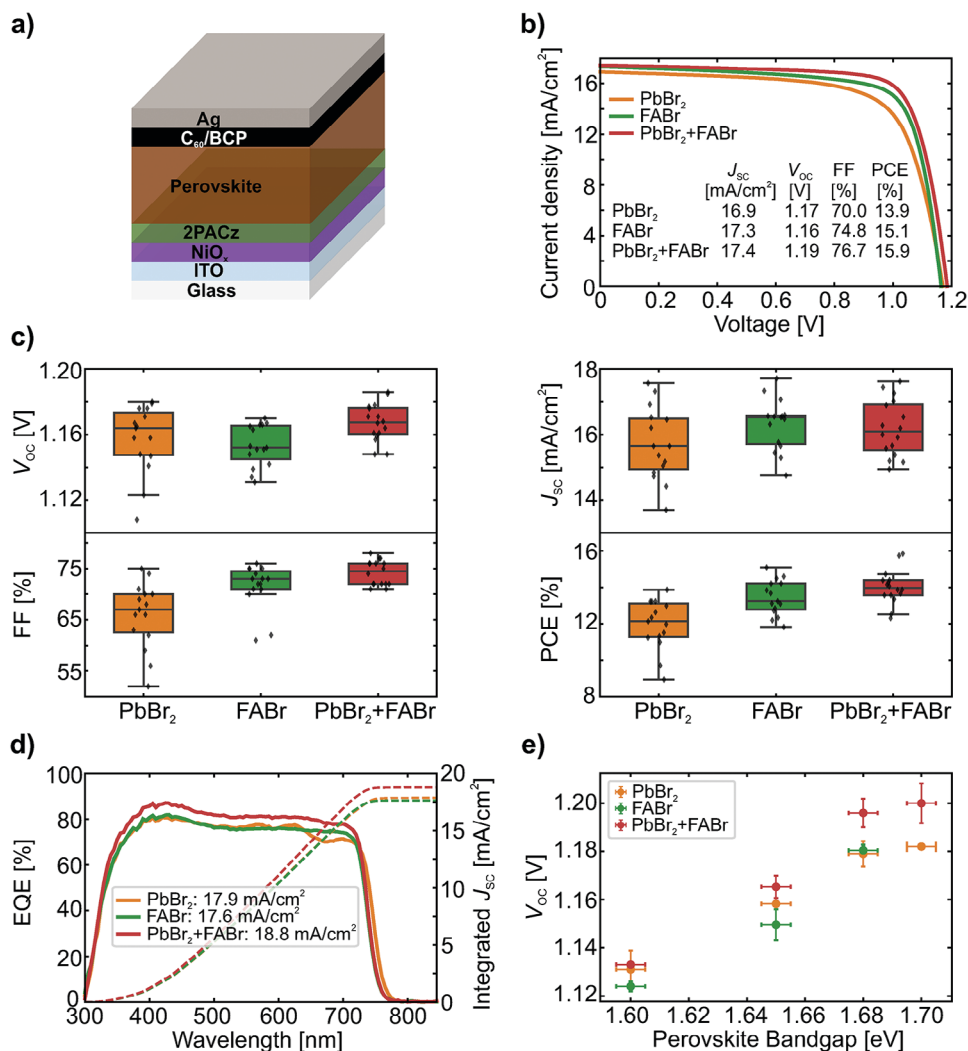


Figure 2. a) Schematic of the perovskite solar cell (PSC) structure (p - i - n) used in this study. b) Current density versus voltage (J - V) characteristics, c) statistical distribution (in total 46 devices) of the open-circuit voltage (V_{oc}), fill factor (FF), short-circuit current density (J_{sc}) and power conversion efficiency (PCE), d) external quantum efficiency (EQE), as well as the corresponding integrated J_{sc} , and e) open-circuit voltage (V_{oc}) as a function of the perovskite bandgap for opaque PSCs with bromide added via the PbBr₂, the FABr or the PbBr₂+FABr process. The PSCs in b–d) have a bandgap of \approx 1.68 eV. In e), the bandgap was varied between 1.60 and 1.70 eV.

the external quantum efficiency (EQE) curves near the absorption edge (maximum of $d(\text{EQE})/d(E)$) according to Krückemeier et al.^[49]

Further details on the fabrication method of the PSCs are described in the Experimental Section.

2.1. Photovoltaic Performance of Perovskite Solar Cells with Engineered Bandgap

Targeting high efficiency and reproducibility, the incorporation of bromide via PbBr₂ and FABr in the first and second deposition step is identified as the superior choice for incorporating bromide in the investigated p - i - n type PSCs.

An enhanced open-circuit voltage (V_{oc}) and fill factor (FF) together with a reduced hysteresis of the devices with incorporated bromide via PbBr₂ and FABr in both deposition steps

(PbBr₂+FABr) are noticeable in the current density–voltage (J - V) characteristics and PV parameters of the best-performing cells (Figure 2b, Figure S4 and Table S1, Supporting Information). These improvements result in a champion performance of 15.85% in the backward scan (15.10% in the forward scan) with a V_{oc} of 1.19 (1.18) V, a J_{sc} of 15.85 (15.10) mAcm⁻², and a FF of 76.7% (73.5%) as depicted in Figure S4d (Supporting Information). A notable hysteresis effect is observed when bromide is incorporated via FABr in the second deposition step (FABr, Figure S4c, Supporting Information). Figure 2c presents the statistical performance of the PSCs in the backward scan. Upon all PV parameters, the increase in FF in the devices with combined bromide incorporation in both deposition steps is particularly striking in the statistical results. In addition, the V_{oc} and the J_{sc} are enhanced, increasing the overall performance of the PSCs. It should be noted that the V_{oc} enhancement is not governed by an increase in the bandgap (Figure S9, Supporting Information).

Instead, it is associated with the mitigation of non-radiative recombination, which will be elaborated upon in the subsequent discussion. Based on a statistical analysis using the *Welch's t test*, statistically significant deviations are observed in both FF and PCE between the devices with combined bromide incorporation in both deposition steps and those with bromide incorporation in only one deposition step (Table S2, Supporting Information). The reduced dispersion of the statistical results of the devices with combined bromide incorporation in both deposition steps suggests an improved reproducibility of the PSCs.

A wider bandgap – obtained by bromide incorporation – raises the possibility of halide segregation, detrimental to device stability.^[4,6] Nevertheless, the strategies employed for bromide incorporation in this study result in stable PSC performance under constant illumination for 5 min at a constant voltage close to the maximum power point (MPP) (Figure S7, Supporting Information). The aspect of long-term stability should be taken into careful consideration in future studies, as it is the primary obstacle that must be overcome before achieving commercialization of PSCs.^[50]

The impact of the different bromide incorporation strategies on charge carrier extraction becomes evident when examining the external quantum efficiency (EQE) in conjunction with the absorption spectra (Figure 2d; Figure S6b, Supporting Information). Particularly in the short wavelength range, the EQE shows a notable decline with the incorporation of bromide in one deposition step compared to the narrow bandgap reference devices with integrated J_{SC} 's of 17.9 and 17.6 mAcm^{-2} for PbBr_2 and FABr PSCs, respectively (Figure S6a, Supporting Information). However, this characteristic can be mitigated if bromide is incorporated in both deposition steps leading to an enhanced integrated J_{SC} of 18.8 mAcm^{-2} . Given that both the device architecture and the absorption spectra (Figure S6b, Supporting Information) remain comparable across all bromide incorporation strategies, the decrease in EQE can possibly be attributed to constrained charge carrier extraction in the case of bromide incorporation in only one deposition step. Thus, it can be concluded that the combined incorporation of bromide in both deposition steps enables an improvement of the charge carrier extraction. Notably, by studying various bandgaps between 1.55 eV and ≈ 1.7 eV, it can be noted in particular that the augmented EQE reduction due to bromide incorporation in one deposition step is already apparent for $E_g \gtrsim 1.6$ eV (Figures S1a and S2a, Supporting Information). This effect is strongly suppressed for the devices with combined bromide incorporation in both deposition steps (Figure S3a, Supporting Information). Impressively, PSCs with incorporated bromide in both deposition steps demonstrate an improvement in V_{OC} for all studied bandgaps ($E_g = 1.60 - 1.70$ eV) compared to the devices with incorporation of bromide in one deposition step (Figure 2e). This behavior is mainly attributed to reduced non-radiative recombination losses and an improved energetic alignment with the charge transport layer and thus reduced recombination at the interface.^[51]

2.2. Material and Photophysical Properties

To quantify the reduction of non-radiative recombination losses in the perovskite thin films processed by combined incorpora-

tion of bromide in both deposition steps ($\text{PbBr}_2 + \text{FABr}$), photoluminescence quantum yield (PLQY) measurements along with the determined internal quasi-Fermi level splitting (QFLS) are employed. From the QFLS one can calculate the 'implied V_{OC} ' (V_{OC-imp}) as described by Stolterfoht et al.^[52] and Fassel et al.^[53]

Half-stack devices with and without electron transport layer (ETL) (in this case C_{60}) are prepared. Analysis of the PLQY and the V_{OC-imp} for the half stack without C_{60} (ITO/ NiO_x /2PACz/perovskite) allows identification of whether non-radiative recombination at the HTL/perovskite limits the V_{OC} of the presented PSCs.^[51,52,54] Remarkable are the high average PLQY (Figure 3a) and V_{OC-imp} (Figure 3b) being well above the obtained V_{OC} of all PSCs presented in Figure 2c. This indicates that the perovskite films exhibit a high optoelectronic quality and that the 2PACz/perovskite interface does not constrain the V_{OC} of the PSCs. For the films with combined bromide incorporation in both deposition steps, the PLQY is improved and the V_{OC-imp} is enhanced by > 10 mV compared to the films processed by incorporating bromide in one deposition step, hinting toward improved bulk properties of these films.

Progressing towards the final device architecture and adding a C_{60} ETL, the PLQY decreases due to pronounced interfacial recombination at the perovskite/ C_{60} interface, consistent with previous reports.^[55–58] However, this fullerene-induced charge carrier quenching is not significantly pronounced, with only a minor reduction in the PLQY (less than one order of magnitude) and the V_{OC-imp} (Figure 3a,b, respectively). It can be concluded that the perovskite/ C_{60} interface does not considerably limit the V_{OC} and is already of good quality in contrast to previous reports for wide bandgap PSCs.^[58] Still, a slightly higher PLQY and V_{OC-imp} can be observed with the combined incorporation of bromide in both deposition steps. The dominant contribution responsible for the enhancement of PLQY originates from the perovskite bulk, rather than the perovskite/ C_{60} interface. The observed trend is in line with that observed for the device V_{OC} , as illustrated in Figure 2c, while the absolute values are ≈ 70 meV smaller as compared to V_{OC-imp} .

To evaluate the impact of reduced trap-state density on the device performance, intensity-dependent PLQY measurements are conducted. The calculated V_{OC-imp} is utilized to extract the internal ideality factor (n_{id}), which hinges on the properties of both bulk and interfacial recombination processes.^[6,52,59–61] First, the half-layer stacks without C_{60} are analyzed (Figure S10, Supporting Information) and a reduction of n_{id} from 1.39 for the films with bromide incorporation in the first deposition step (PbBr_2) and bromide incorporation in the second deposition step (FABr) to 1.36 for the films with combined bromide incorporation in both deposition steps ($\text{PbBr}_2 + \text{FABr}$) can be observed. The stacks with ETL (C_{60}) show a very similar trend, with a slight reduction of the n_{id} from 1.56 for the films with bromide incorporation in the second deposition step (FABr) to 1.54 for the films with bromide incorporation in the first deposition step (PbBr_2). The lowest n_{id} (1.52) can be obtained for the films with combined bromide incorporation in both deposition steps ($\text{PbBr}_2 + \text{FABr}$). This result is consistent with the improved FF and V_{OC} obtained from the statistical results of the combined bromide incorporation in both deposition steps (Figure 2c; Table S1, Supporting Information).

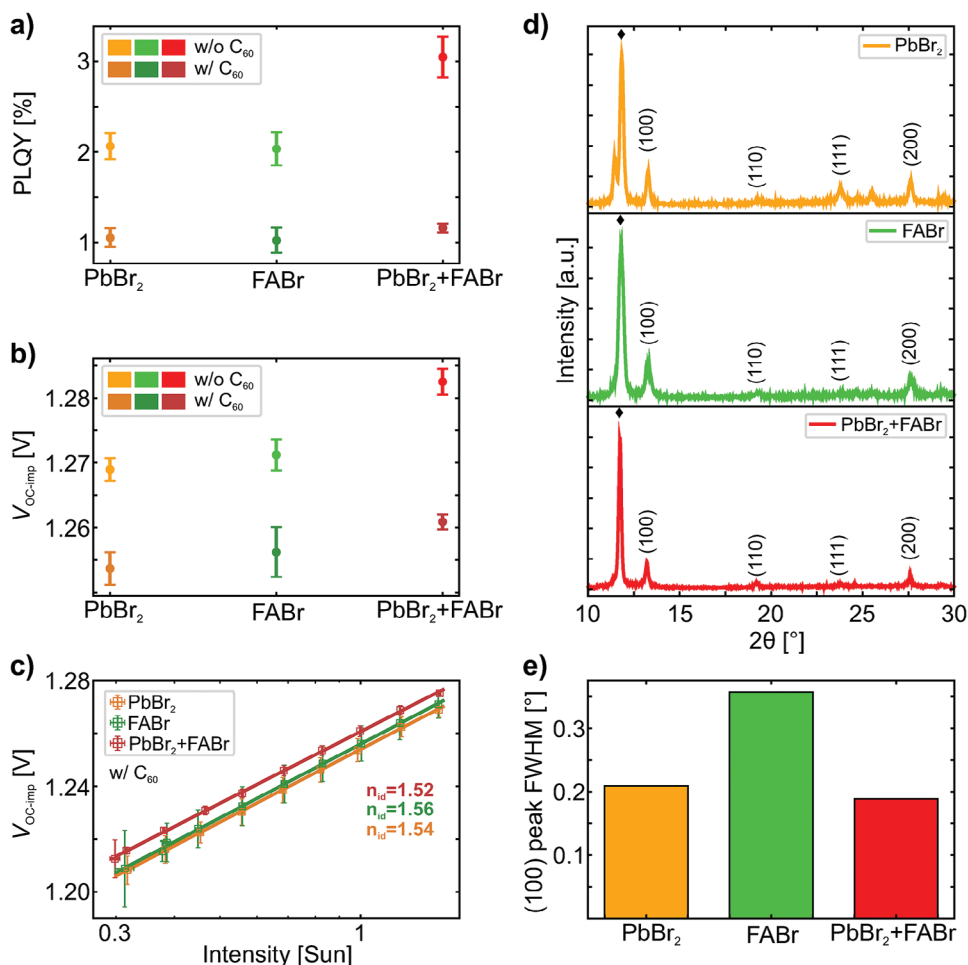


Figure 3. a) Photoluminescence quantum yield (PLQY), b) the obtained implied V_{OC} (V_{OC-imp}), c) the ideality factor (n_{id}) extracted from a fit to the V_{OC-imp} (derived from intensity-dependent PLQY measurements) measured with C_{60} ETL, d) the XRD pattern (\blacklozenge denotes the PbI_2 phase) and e) the FWHM of the (100) perovskite peak of the perovskite films with bromide added via the $PbBr_2$, the FABr or the $PbBr_2$ +FABr process fabricated on $ITO/NiO_x/2PACz$ substrates. a–c) are measured from the HTL side.

X-ray diffraction (XRD) measurements, as well as scanning electron microscope (SEM) images reveal an improved crystalline growth and morphology of the perovskite layer with combined bromide incorporation in both deposition steps. The XRD measurements indicate that all three incorporation strategies result in perovskite crystals with similar orientation, showing main diffraction peaks at $\approx 13.3^\circ$ and $\approx 27.6^\circ$, corresponding to the (100) and (200) planes of the cubic-phase perovskite, respectively (Figure 3d). Upon comparing the peak structures, it becomes evident that for the incorporation of bromide via $PbBr_2$, a distinct double peak structure of the PbI_2 peak at approximately $\approx 12.4^\circ$ is observable. The double peak structure indicates a halide phase segregation and a non-uniform distribution of the bromide in the final perovskite film.^[62] All three bromide incorporation strategies exhibit a noticeable PbI_2 peak, which is more pronounced compared to the (100) perovskite peak. This is attributed to a larger amount of unreacted PbI_2 , which has been observed in previous reports^[14,63,64] using the solution-based two-step method. Examining the full width at half maximum (FWHM) of the (100) perovskite peak displayed in Figure 3e, a decreased value is evi-

dent for the combined bromide incorporation in both deposition steps (0.189°), in contrast to bromide incorporation via $PbBr_2$ (0.209°) or FABr (0.357°). The reduced FWHM value indicates an enhanced crystallinity and larger grain sizes of the perovskite film according to the Scherrer equation

$$D = \frac{K\lambda}{\beta \cos(\Theta)} \quad (1)$$

where D is the crystallite size, K a constant, λ the X-ray wavelength, β the FWHM and Θ the diffraction angle.^[38,65]

According to the SEM images (Figure S11, Supporting Information), all perovskite films (Ref, $PbBr_2$, FABr, and $PbBr_2$ +FABr) exhibit a comparable morphology, yet subtle distinctions are discernible. The reference films and the films with $PbBr_2$ display more pinholes and present a disorderly appearance in contrast to the films with FABr and the films with $PbBr_2$ and FABr. Furthermore, an augmented presence of light grains, attributable to unreacted PbI_2 , is observable in line with XRD results. Enhanced crystalline growth and a more ordered surface

morphology are obtained for the films with FABr and the films with PbBr₂ and FABr. However, the films with FABr display additional microwrinkles, resulting in a superior surface quality for the films with PbBr₂ and FABr.

In summary, material characterization reveals that the combined incorporation of bromide in both deposition steps reduces non-radiative recombination losses and results in an improved film quality of the perovskite layer.

2.3. Toward Highest Power Conversion Efficiency

Compositional engineering and surface passivation are pursued to further improve the film quality and enhance the J_{SC} of the two-step solution-processed PSC, targeting high PCEs suitable for integration into a monolithic tandem configuration. Here, wide bandgap PSCs with combined bromide incorporation in both deposition steps (PbBr₂+FABr, labeled now as Control) are used as a means of choice to further advance the PCE. For compositional engineering, CsI is added in the bulk, while LiF is used as surface passivation.

Employing CsI in the bulk by adding an optimized amount of CsI in the inorganic precursor solution (7 mol.% CsI) leads to an increase in the J_{SC} by an average of 2–3 mAcm⁻² compared to the Control devices (Figures S13a and S13b, Supporting Information). This enables improved current matching in monolithic perovskite/silicon TSCs.^[66] However, at the same time the addition of CsI results in a significant reduction in V_{OC} by an average of 30–40 mV (Figures S13a and S13b, Supporting Information). This is consistent with the observed reduction in the PLQY and V_{OC-imp} (Figures S18a and S18b, Supporting Information). To counteract the reduction in V_{OC} while maintaining the improved J_{SC} , 1 nm of LiF is applied as a surface passivation.^[58,67] **Figure 4a** shows the statistical performance of PSCs without any modification (Control) and with 7 mol.% CsI added in the inorganic precursor solution together with 1 nm LiF as surface passivation (labeled as CsI+LiF). Using this strategy, the V_{OC} is successfully recovered and even increased by an average of 20–30 mV compared to the Control devices (Figure 4a,b; Figure S13, Supporting Information). This leads to an average enhancement of the PCE from 15.9% for the Control PSCs to 18.5% for the CsI+LiF PSCs (Figure 4a). The enhancement in V_{OC} and FF for the devices with CsI and LiF is also highlighted by the lowest obtained n_{id} of 1.44 (Figure S18d, Supporting Information, with ETL interface). It has to be noted that the enhancement in V_{OC} does not correspond to an increase in the bandgap (Figure S15, Supporting Information). Performing a *Welch's t test* (Table S4, Supporting Information) highlights the improvement in J_{SC} and V_{OC} for the devices with added CsI and LiF, as they differ statistically significant from the Control devices. As a result, the PSCs with CsI and LiF profit from the J_{SC} increase from the CsI added in the bulk and the enhancement in V_{OC} via LiF surface passivation. The champion device exhibits a PCE of 18.54% in the backward scan (17.42% in the forward scan), a V_{OC} of 1.20 (1.19) V, a J_{SC} of 19.80 (19.76) mAcm⁻², and a FF of 78.1% (73.9%) (Figure 4b; Figure S12a, Supporting Information). The summarized $J-V$ results can be found in Table S3 (Supporting Information).

Existing literature suggests that LiF has the potential to serve as a field effect passivator, likely overcompensating the enhanced

defect density in the first monolayers of the C60 and thus enabling a higher V_{OC} .^[67] This in turn leads to an overall improvement in the photovoltaic performance of the device.

As evident from the EQE spectrum (Figure S13c, Supporting Information), addition of CsI improves the charge carrier extraction, which is only slightly negatively affected by using LiF as surface passivation (Figure 4c). It is noted that the enhancement in the EQE spectrum cannot be explained by an increased absorption (Figure S14, Supporting Information).

The SEM images (Figure 4d,e; Figure S16, Supporting Information) reveal information about the morphology of the perovskite films. Addition of CsI leads to a slightly lower density of bright grains that can be related to less PbI₂-rich crystallites.^[55] This assumption is supported by XRD measurements (Figure S17a, Supporting Information), where CsI films exhibit an increased ratio of the (100) perovskite peak to the PbI₂ peak. A similar effect has already been reported in previous studies.^[68–70] Additionally, the introduction of CsI results in slightly enlarged grain sizes, enhancing the charge carrier extraction.^[71,72] By incorporating LiF for surface passivation in films along with CsI added in the bulk, a more structured surface morphology with larger grain sizes emerges, similar to what is observed in films with only CsI (Figure 4e; Figure S16, Supporting Information).

The addition of CsI and LiF does not impair the short-term stability as confirmed by MPP tracking for 5 min (Figure S12c, Supporting Information). However, it is known from literature that LiF has a negative impact on long-term operational stability.^[65,73] For this reason, alternative surface passivation strategies that do not impair stability should be the goal of future studies.

2.4. Implementation in 2T Tandem Devices

After successfully testing the incorporation of bromide into single-junction PSCs and thereby increasing the bandgap up to 1.68 eV, the developed strategy is employed for fabrication of planar monolithic perovskite/silicon TSCs. The device architecture of the TSCs consists of the layer stack silicon/ITO/NiO_x/2PACz/perovskite/C₆₀/SnO₂/IZO/Ag/MgF₂ with an active area of 1.0 cm². The $J-V$ characteristic and EQE response of the champion device are depicted in **Figure 5**, which exhibits good performance and high voltages. The best tandem device with an active area of 1.0 cm² exhibits a PCE of 23.73% in the backward scan (21.89% in the forward scan), a V_{OC} of 1.85 (1.82) V, a J_{SC} of 17.11 (16.97) mAcm⁻², and a FF of 74.9% (71.0%) (Figure 5a). The V_{OC} is already in the expected range based on the results for the single-junction PSC and the silicon cell. The performance is mainly limited by low FF that requires further investigation and optimization. The $J-V$ characteristic reveals a hysteresis index of 7.81% between backward and forward scan. EQE spectra are employed to investigate the integrated J_{SC} of the tandem device (Figure 5b). The J_{SC} of the perovskite top cell (17.71 mAcm⁻²) is slightly lower than the J_{SC} of the silicon bottom cell (17.82 mAcm⁻²), but are close to current-matching. The integrated J_{SC} of the tandem is in good agreement with the result from the $J-V$ curve. Short-term stability is confirmed by MPP tracking for 5 min (Figure S19, Supporting Information).

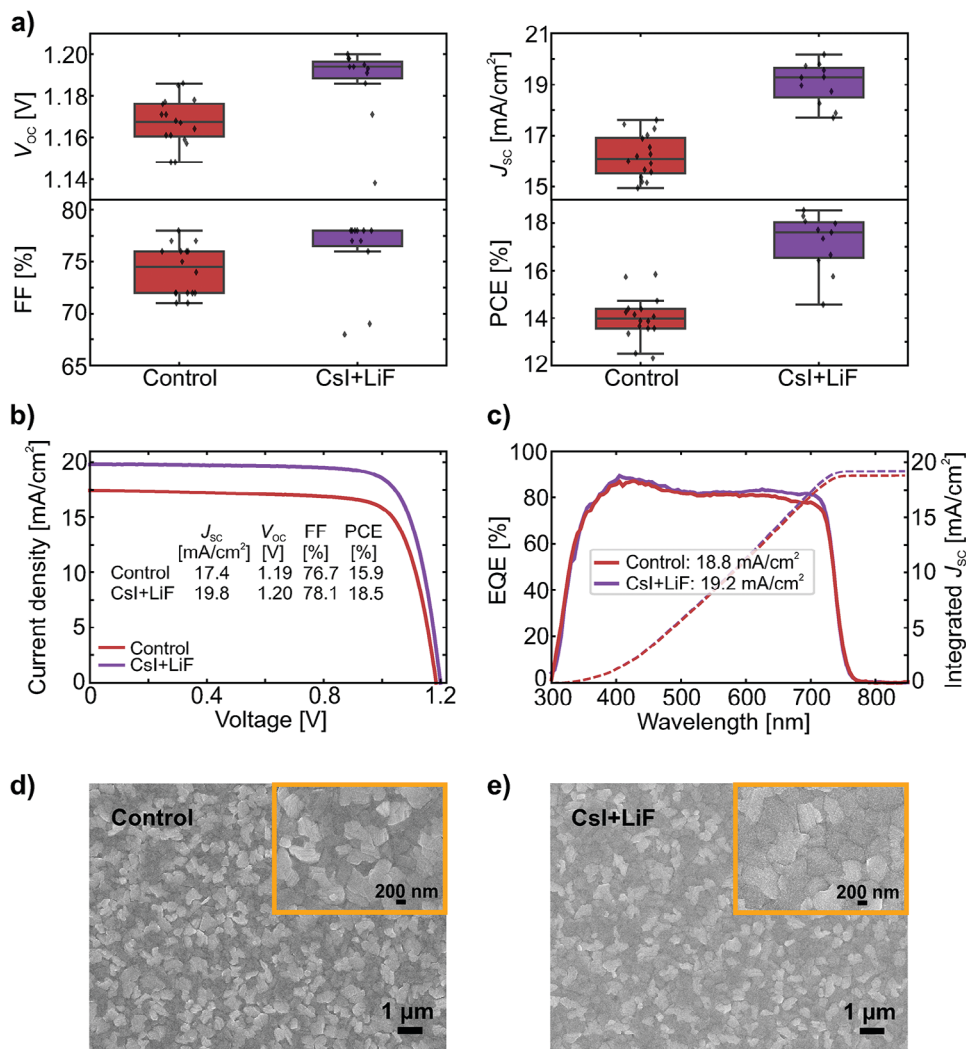


Figure 4. a) Statistical distribution of the open-circuit voltage (V_{OC}), fill factor (FF), short-circuit current density (J_{SC}) and power conversion efficiency (PCE), b) current density versus voltage (J - V) characteristics, c) external quantum efficiency (EQE), as well as the corresponding integrated J_{SC} for opaque perovskite solar cells (PSCs) and d,e) top-view scanning electron microscopy (SEM) images of perovskite films of the wide bandgap PSCs (bromide incorporated via $PbBr_2$ and FABr) without (labeled as Control) and with CsI added in the inorganic precursor solution (7 mol.% CsI) and LiF as surface passivation (1 nm) (labeled as CsI+LiF).

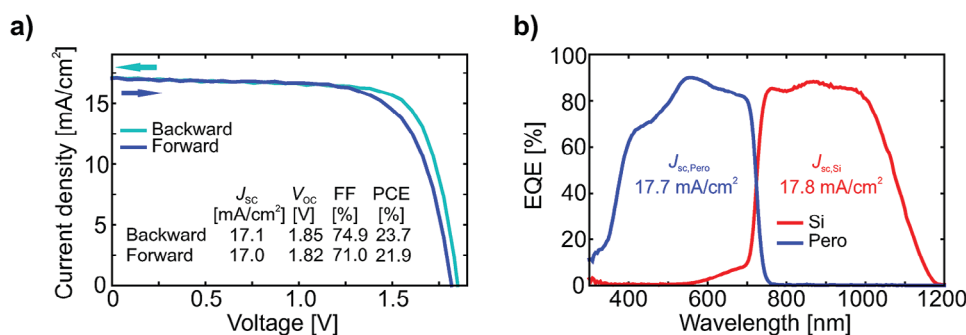


Figure 5. a) Current density versus voltage (J - V) characteristic and b) external quantum efficiency (EQE) of the champion monolithic 2T TSC (active area: 1.0 cm²) with a perovskite bandgap of $E_g = 1.68$ eV (bromide incorporated via $PbBr_2$ and FABr) with added CsI in the bulk (7 mol.%) and 1 nm LiF as surface passivation and with 90 nm of MgF_2 as antireflective coating.

The results indicate a straightforward implementation of the elaborated strategy on 2T TSCs.

3. Conclusion

This work presents a novel and effective strategy for the incorporation of bromide into wide bandgap PSCs fabricated via the solution-based two-step method. A combined incorporation of bromide in both deposition steps via PbBr_2 and FABr shows a substantial enhancement in charge carrier extraction and quasi-Fermi level splitting compared to films with incorporation of bromide in either the first or the second deposition step. Further compositional engineering by adding CsI in the bulk and using LiF as surface passivation leads to improved optoelectronic properties, pushing the efficiency from 15.9% up to 18.5%. This improvement in performance is mainly attributed to an enhanced crystallinity of the perovskite films and therefore enhanced charge carrier extraction. To the best of our knowledge, this is the most efficient *p-i-n* type PSC with a bandgap of 1.68 eV, which is processed via a two-step spin-coating method. Employing these strategies in monolithic perovskite/silicon TSCs (active area of 1 cm^2) result in high efficiencies up to 23.7%. Overall, this work introduces a successful strategy for producing high-performance and reproducible *p-i-n* type wide bandgap (PSCs) and planar perovskite/silicon (TSCs) using a two-step spin-coating technique.

4. Experimental Section

Materials: 2PACz (TCI, CAS: 20999-38-6), Lead iodide (PbI_2 : TCI, CAS: 10101-63-0), Lead bromide (PbBr_2 : TCI, CAS: 10031-22-8), Formamidinium iodide (FAI: Greatcell solar materials, CAS: 879643-71-7), Formamidinium bromide (FABr: Dyenamo, CAS: 146958-06-7), Methylammonium iodide (MAI: Dyenamo, CAS: 14965-49-2), Methylammonium chloride (MACl: Dyenamo, CAS: 593-51-1), Cesium iodide (CsI: Alfa Aesar, CAS: 7647-17-8), Fullerene- C_{60} (C_{60} : Sigma-Aldrich, CAS: 99685-96-8), Bathocuproine (BCP: Lumtec, CAS: 4733-39-5), Magnesium fluoride (MgF_2 : Sigma-Aldrich, CAS: 7783-40-6), Lithium fluoride (LiF: ChemPur, CAS: 7789-24-4). All solvents including N,N-dimethylformamide, 99.8% (DMF, CAS: 68-12-2), Dimethyl sulfoxide anhydrous, $\geq 99.9\%$ (DMSO, CAS: 67-68-5), 2-Propanol, 99.5%, (IPA, CAS: 67-63-0) were ordered from Sigma-Aldrich. Ethanol (EtOH) absolute anhydrous, $\geq 99.8\%$ was ordered from VWR Chemicals.

Perovskite Solution Preparation: The reference double cation perovskite solution was prepared according to Gutierrez-Partida et al.^[48] Two different solutions were prepared. The first solution was prepared by dissolving 1.5 M PbI_2 (691.55 mg) in 1 mL DMF:DMSO (9:1 volume ratio, v:v). The organic cation solution was prepared by dissolving FAI (90 mg), MAI (6.4 mg) and MACl (9 mg) in 1 mL IPA. The inorganic solution was heated up to 130°C for 30 min to completely dissolve the materials. The addition of MACl improves the crystallization of the perovskite film but evaporates in the final annealing step.^[74]

The wide bandgap double cation perovskites were prepared differently depending on the bromide incorporation strategy. In the case of bromide incorporation via PbBr_2 , 1.07 M PbI_2 and 0.43 M PbBr_2 were dissolved in 1 mL DMF:DMSO (9:1 volume ratio, v:v). Here, the reference cation solution was taken. In the case of bromide incorporation via FABr, the reference PbI_2 solution was used. The organic cation solution was prepared by dissolving FAI (19.5 mg), FABr (51.3 mg), MAI (6.4 mg), and MACl (9 mg) in 1 mL IPA. For the incorporation of bromide via PbBr_2 and FABr, 1.275 M PbI_2 , and 0.225 M PbBr_2 were dissolved in 1 mL DMF:DMSO (9:1 volume ratio, v:v). The organic cation solution was prepared by dis-

solving FAI (51.6 mg), FABr (27.9 mg), MAI (6.4 mg), and MACl (9 mg) in 1 mL IPA. All inorganic solutions were heated up to 130°C for 30 min to completely dissolve the materials.

In the case of the wide bandgap perovskites with additional CsI, the inorganic solution was prepared as mentioned before for the PbBr_2 +FABr solution (less DMSO, since it was added with the CsI solution) and heated up to 130°C for 30 min to completely dissolve the materials. After cooling down, 70 μL CsI solution (corresponds to 7 mol.% CsI, 390 mg mL^{-1} CsI in DMSO) was added to the inorganic solution. The cation solution remained unchanged.

Single-Junction Perovskite Solar Cell Fabrication: The planar *p-i-n* type PSCs with the layer stack glass/ITO/ NiO_x /2PACz/perovskite/ C_{60} /BCP/Ag were fabricated as follows. The glass substrates with 120 nm thick indium tin oxide (ITO) coating (sheet resistance $15 \Omega\text{cm}^{-2}$, Luminescence Technology, CAS: 50926-11-9) were cut in $16 \text{ mm} \times 16 \text{ mm}$ and cleaned in an ultrasonic bath with deionized (DI) water with glass cleaner, acetone and IPA for 10 min each. This is followed by 3 min of oxygen plasma treatment before the deposition of the hole transport (HTL) layer. For the HTL layer, a 5 nm thick NiO_x film was sputtered from a NiO_x target using 100 W power with pure Ar at 1 mTorr on the ITO substrate. Then, a thin layer of 2PACz was deposited on the ITO/ NiO_x substrate by spin-coating at 3000 rpm for 30 s and subsequently annealed at 100°C for 10 min. The 2PACz precursor solution was prepared by dissolving 2PACz in anhydrous EtOH with a concentration of 0.375 mg mL^{-1} . The prepared solution was placed in an ultrasonic bath for at least 20 min before use. All perovskite absorber layers were deposited on the substrate with the solution-based two-step deposition method. The first step was the deposition of the inorganic PbI_2 layer. This was achieved by dropping 60 μL of the lead iodide solution and spin-coating at 1500 rpm for 30 s. The films were subsequently annealed at 70°C for 1 min resulting in a yellow-transparent layer. The formation of the perovskite was achieved by dropping 80 μL of the cation solution on top of the lead iodide layer and rapidly starting the spin-coating process at 2500 rpm for 30 s, which resulted in a red film. This was followed by an annealing step at 150°C for 15 min outside of the glovebox under ambient conditions (at a relative humidity of 20–50%) converting it to the desired black perovskite film. It had to be noted that the spincoating process took place in a N_2 -filled glovebox. For the second annealing step, a transport-box was used to transfer the samples out of the glovebox in order to keep the samples in a nitrogen atmosphere right before the annealing on a preheated plate (150°C). As soon as the transport-box was opened, the crystallization and phase-change process started and a rapid transfer to the hotplate directly after opening the transport-box was beneficial for the cell performance.^[48] After annealing, 1 nm LiF was thermally evaporated at an evaporation rate of $0.1\text{--}0.2 \text{ \AA s}^{-1}$ at a pressure of around 10^{-6} mbar for the samples with LiF as surface passivation. As electron transport (ETL) layer, 20 nm of C_{60} and 5 nm of BCP were thermally evaporated and deposited using an Angstrom evaporation system at an evaporation rate of $0.1\text{--}0.2 \text{ \AA s}^{-1}$ at a pressure of around 10^{-6} mbar. Subsequently, 100 nm Ag was thermally evaporated using a shadow mask to define the active area to 10.5 mm^2 and complete the PSCs with four pixels per substrate.

Perovskite/Silicon Tandem Solar Cell Fabrication: Before depositing the HTL layer, the silicon solar cells ($25 \text{ mm} \times 25 \text{ mm}$) were cleaned with acetone and IPA in a spincoater process. For the HTL layer, a 5 nm thick NiO_x film was sputtered from a NiO_x target on the silicon bottom cell with ITO layer. This was followed by a thin 2PACz layer deposited as mentioned above with a higher concentrated 2PACz solution with 0.475 mg mL^{-1} . The perovskite absorber layer was fabricated as mentioned above, using 130 μL of the lead iodide solution and 150 μL of the cation solution. After annealing, 1 nm LiF was thermally evaporated as surface passivation. For the ETL layer, 20 nm of C_{60} was thermally evaporated. A 35 nm SnO_2 layer prepared by atomic layer deposition (ALD) was used as buffer layer. Subsequently, 90 nm sputtered IZO from a IZO target using 190 W power with pure Ar and O_2 at 1 mTorr was used as a transparent electrode and the active area of 1.04 cm^2 was defined by the thermally evaporated Ag electrode (300 nm). In order to reduce the reflection losses, 90 nm MgF_2 as an antireflection layer was evaporated on top of the Ag.

Solar Cell Characterization: The *J-V* characteristics of the PSCs were measured with a class AAA xenon-lamp solar simulator (Newport Oriel

Sol3A) with a scan rate set at 0.6 Vs⁻¹ using a sourcemeter (Keithley 2400) with an air-mass 1.5 global (AM1.5G) spectra (100 mWcm⁻²). The solar simulator irradiation intensity was calibrated using a certified silicon solar cell (Fraunhofer ISE) equipped with a KG5 band pass filter. The stabilized PCE of the PSCs was determined by measuring the photocurrent at the maximum power point (MPP) by using a perturb and observing algorithm under continuous AM 1.5G illumination, while the temperature of the devices was controlled at 25 °C by a Peltier element connected to a microcontroller during the measurements. For measuring with the solar simulator, a shadow mask with an area of 7.84 mm² was used for the single-junction PSCs and with an area of 1.0 cm² for the 2T TSCs. To evaluate the data, a mismatch factor was determined from the EQE curve and the solar simulator spectrum and the *J*–*V* curves were corrected accordingly. The EQE was measured using a PVE300 photovoltaic QE system (Bentham EQE system). A chopping frequency in the range of 560–590 Hz with an integration time of 500 ms (750 ms for 2T tandems) to acquire the spectra in a wavelength range from 300 to 850 nm (300 to 1200 nm for 2T tandems) was used. An illumination spot (0.74 mm for single-junction, 1.5 mm for 2T tandems) was utilized to obtain the average over possible variations in the EQE spectra. For measuring the EQE, a shadow mask with an area of 1.0 cm² was used for the 2T TSCs. The solar simulator and EQE measurements were performed in a N₂-filled glovebox.

Perovskite Film Characterization: SEM analyzes were carried out in a scanning electron microscope (Zeiss LEO1530) with an in-lens detector and a aperture size of 20–30 μm. For cross-sectional analyzes, the cross-sections were covered with a 3 nm thick platinum layer deposited by sputtering to prevent charging. The applied acceleration voltages for surface and cross-sectional analyzes range between 5 and 10 kV. Transmittance and reflectance spectra of the perovskite thin films were measured using a PerkinElmer Lambda1050 spectrophotometry setup equipped with a double-monochromator and a modulated source. A chopper frequency of 46 Hz was applied. The crystal structure of the perovskite layers was carried out utilizing XRD (Bruker D2Phaser system) with Cu-K_α radiation (λ = 1.5405 Å) in Bragg–Brentano configuration using a LynxEye detector. The XRD was taken from the perovskite layer deposited on the ITO/NiO_x/ZPACz substrate to obtain the same perovskite nucleation, as well as crystallization as in the solar cells. PLQY measurements were carried out using a LuQY Pro setup from QYB. The samples were mounted inside an integrating sphere and a green laser (λ = 532 nm) was directed into the sphere via a small entrance port. The radiative limit of the V_{OC} (V_{OC-rad}) and the implied V_{OC} (V_{OC-imp}) were determined from the (intensity-dependent) PLQY measurements as described by Stolterfoht et al.^[52] and Kirchartz et al.^[49] From the quasi-Fermi level splitting (QFLS, E_F) one can calculate the ‘implied V_{OC}’ via

$$V_{OC-imp} = \frac{\Delta E_F}{q} = V_{OC-rad} + \frac{k_B T}{q} \ln \left(PLQY \frac{J_G}{J_{0-rad}} \right) \quad (2)$$

where V_{OC-rad} is the radiative limit, k_B the Boltzmann constant, *T* the temperature, *q* the elemental charge, J_G the generation current density and J_{0-rad} the radiative thermal recombination current density in the dark. The internal ideality factor (n_{id}) was determined from these measurements as a fit to the calculated V_{OC-imp}.^[52,53] All perovskite film characterization methods were performed in ambient air conditions.

Statistical Analysis: To check the deviation of the statistical results from each other, *Welch’s t test* was applied. *Welch’s t test* is an adaption of the *Student’s t test*^[75] and is more reliable when the two samples have unequal variances and possibly unequal sample sizes.^[76,77] These tests are often referred to as “independent samples” or “unpaired” *t* tests because they are usually applied when the statistics underlying the two samples being compared do not overlap. It is assumed that the sample means for the two samples being compared are normally distributed.^[75] The *t* statistic for testing whether the results differ from each other or not can be calculated as follows:

$$t = \frac{\bar{X} - \bar{Y}}{\sqrt{\frac{S_x^2}{n_x} + \frac{S_y^2}{n_y}}} \quad (3)$$

whereas \bar{X} and \bar{Y} are the mean values, S_x and S_y the standard deviations and n_x and n_y the sample sizes.

Supporting Information

Supporting Information is available from the Wiley Online Library or from the author.

Acknowledgements

Financial support by the Initiating and Networking funding of the Helmholtz Association (Project Zeitenwende and the Solar Technology Acceleration Platform (Solar TAP)), the program oriented funding IV of the Helmholtz Association (Materials and Technologies for the Energy Transition, Topic 1: Photovoltaics and Wind Energy, Code: 38.01.04), the German Federal Ministry for Economic Affairs and Climate Action (BMWK) through the project 27Plus6 (03EE1056B), and the Karlsruhe School of Optics and Photonics (KSOP) is gratefully acknowledged. The authors thank the whole “perovskite task force” at KIT for fruitful discussions and assistance. The primary author expresses gratitude to Hang Hu and Thomas Feeney for their execution of ALD, and acknowledges Sören Ihssen for providing assistance with Python programming.

Open Access funding enabled and organized by Projekt DEAL.

Conflict of Interest

The authors declare no conflict of interest.

Data Availability Statement

The data that support the findings of this study are available from the corresponding author upon reasonable request.

Keywords

2T tandem solar cells, bandgap engineering, perovskite solar cells, sequential deposition

Received: September 20, 2023

Published online:

- [1] T. Niewelt, B. Steinhauser, A. Richter, B. Veith-Wolf, A. Fell, B. Hammann, N. Grant, L. Black, J. Tan, A. Youssef, J. Murphy, J. Schmidt, M. Schubert, S. Glunz, *Sol. Energy Mater. Sol. Cells* **2022**, 235, 111467.
- [2] National Renewable Energy Laboratory, Best Research-Cell Efficiency Chart, <https://www.nrel.gov/pv/cell-efficiency.html>, (accessed: June, 2023).
- [3] H. Shen, D. Walter, Y. Wu, K. C. Fong, D. A. Jacobs, T. Duong, J. Peng, K. Weber, T. P. White, K. R. Catchpole, *Adv. Energy Mater.* **2019**, 10, 1902840.
- [4] J. Tong, Q. Jiang, F. Zhang, S. B. Kang, D. H. Kim, K. Zhu, *ACS Energy Lett.* **2020**, 6, 232.
- [5] S. Gharibzadeh, I. M. Hossain, P. Fassl, B. A. Nejjand, T. Abzieher, M. Schultes, E. Ahlswede, P. Jackson, M. Powalla, S. Schäfer, M. Rienäcker, T. Wietler, R. Peibst, U. Lemmer, B. S. Richards, U. W. Paetzold, *Adv. Funct. Mater.* **2020**, 30, 1909919.

- [6] A. Al-Ashouri, E. Köhnen, B. Li, A. Magomedov, H. Hempel, P. Caprioglio, J. A. Márquez, A. B. M. Vilches, E. Kasparavicius, J. A. Smith, N. Phung, D. Menzel, M. Grischek, L. Kegelmann, D. Skroblin, C. Gollwitzer, T. Malinauskas, M. Jošt, G. Matič, B. Rech, R. Schlatmann, M. Topič, L. Korte, A. Abate, B. Stannowski, D. Neher, M. Stolterfoht, T. Unold, V. Getautis, S. Albrecht, *Science* **2020**, *370*, 1300.
- [7] J. Liu, E. Aydin, J. Yin, M. D. Bastiani, F. H. Isikgor, A. U. Rehman, E. Yengel, E. Ugur, G. T. Harrison, M. Wang, Y. Gao, J. I. Khan, M. Babics, T. G. Allen, A. S. Subbiah, K. Zhu, X. Zheng, W. Yan, F. Xu, M. F. Salvador, O. M. Bakr, T. D. Anthopoulos, M. Lanza, O. F. Mohammed, F. Laquai, S. D. Wolf, *Joule* **2021**, *5*, 3169.
- [8] J. Xu, C. C. Boyd, Z. J. Yu, A. F. Palmstrom, D. J. Witter, B. W. Larson, R. M. France, J. Werner, S. P. Harvey, E. J. Wolf, W. Weigand, S. Manzoor, M. F. A. M. van Hest, J. J. Berry, J. M. Luther, Z. C. Holman, M. D. McGehee, *Science* **2020**, *367*, 1097.
- [9] M. D. Bastiani, G. Armaroli, R. Jalmoood, L. Ferlauto, X. Li, R. Tao, G. T. Harrison, M. K. Eswaran, R. Azmi, M. Babics, A. S. Subbiah, E. Aydin, T. G. Allen, C. Combe, T. Cramer, D. Baran, U. Schwingenschlögl, G. Lubineau, D. Cavalcoli, S. D. Wolf, *ACS Energy Lett.* **2022**, *7*, 827.
- [10] F. H. Isikgor, F. Furlan, J. Liu, E. Ugur, M. K. Eswaran, A. S. Subbiah, E. Yengel, M. D. Bastiani, G. T. Harrison, S. Zhumagali, C. T. Howells, E. Aydin, M. Wang, N. Gasparini, T. G. Allen, A. U. Rehman, E. V. Kerschaver, D. Baran, I. McCulloch, T. D. Anthopoulos, U. Schwingenschlögl, F. Laquai, S. D. Wolf, *Joule* **2021**, *5*, 1566.
- [11] F. Huang, M. Li, P. Siffalovic, G. Cao, J. Tian, *Energy Environ. Sci.* **2019**, *12*, 518.
- [12] M. Jung, S.-G. Ji, G. Kim, S. I. Seok, *Chem. Soc. Rev.* **2019**, *48*, 2011.
- [13] V. Cimrová, M. Guesmi, S. Eom, Y. Kang, D. Výprachtický, *Materials* **2023**, *16*, 1049.
- [14] Y. Han, H. Xie, E. L. Lim, D. Bi, *Sol. RRL* **2022**, *6*, 2101007.
- [15] B. Chen, P. Wang, R. Li, N. Ren, W. Han, Z. Zhu, J. Wang, S. Wang, B. Shi, J. Liu, P. Liu, Q. Huang, S. Xu, Y. Zhao, X. Zhang, *ACS Energy Lett.* **2022**, *7*, 2771.
- [16] Q. Li, Y. Zhao, W. Zhou, Z. Han, R. Fu, F. Lin, D. Yu, Q. Zhao, *Adv. Energy Mater.* **2019**, *9*, 1902239.
- [17] K. Liang, D. B. Mitzi, M. T. Prikas, *Chem. Mater.* **1998**, *10*, 403.
- [18] D. Bi, S.-J. Moon, L. Häggman, G. Boschloo, L. Yang, E. M. J. Johansson, M. K. Nazeeruddin, M. Grätzel, A. Hagfeldt, *RSC Adv.* **2013**, *3*, 18762.
- [19] J. Burschka, N. Pellet, S.-J. Moon, R. Humphry-Baker, P. Gao, M. K. Nazeeruddin, M. Grätzel, *Nature* **2013**, *499*, 316.
- [20] Q. Jiang, Y. Zhao, X. Zhang, X. Yang, Y. Chen, Z. Chu, Q. Ye, X. Li, Z. Yin, J. You, *Nat. Photonics* **2019**, *13*, 460.
- [21] W. Hui, L. Chao, H. Lu, F. Xia, Q. Wei, Z. Su, T. Niu, L. Tao, B. Du, D. Li, Y. Wang, H. Dong, S. Zuo, B. Li, W. Shi, X. Ran, P. Li, H. Zhang, Z. Wu, C. Ran, L. Song, G. Xing, X. Gao, J. Zhang, Y. Xia, Y. Chen, W. Huang, *Science* **2021**, *371*, 1359.
- [22] P. Ahlawat, A. Hinderhofer, E. A. Alharbi, H. Lu, A. Ummadisingu, H. Niu, M. Invernizzi, S. M. Zakeeruddin, M. I. Dar, F. Schreiber, A. Hagfeldt, M. Grätzel, U. Rothlisberger, M. Parrinello, *Sci. Adv.* **2021**, *7*, eabe3326.
- [23] G. E. Eperon, M. T. Hörantner, H. J. Snaith, *Nat. Rev. Chem.* **2017**, *1*, 12.
- [24] Z. Wang, Z. Song, Y. Yan, S. F. Liu, D. Yang, *Adv. Sci.* **2019**, *6*, 1801704.
- [25] E. Aydin, T. G. Allen, M. D. Bastiani, L. Xu, J. Ávila, M. Salvador, E. V. Kerschaver, S. D. Wolf, *Nat. Energy* **2020**, *5*, 851.
- [26] M. Jošt, E. Köhnen, A. B. Morales-Vilches, B. Lipovšek, K. Jäger, B. Macco, A. Al-Ashouri, J. Krč, L. Korte, B. Rech, R. Schlatmann, M. Topič, B. Stannowski, S. Albrecht, *Energy Environ. Sci.* **2018**, *11*, 3511.
- [27] F. Gota, R. Schmager, A. Farag, U. W. Paetzold, *Opt. Express* **2022**, *30*, 14172.
- [28] S. Mariotti, E. Köhnen, F. Scheler, K. Sveinbjörnsson, L. Zimmermann, M. Piot, F. Yang, B. Li, J. Warby, A. Musienko, D. Menzel, F. Lang, S. Keßler, I. Levine, D. Mantione, A. Al-Ashouri, M. S. Härtel, K. Xu, A. Cruz, J. Kurpiers, P. Wagner, H. Köbler, J. Li, A. Magomedov, D. Mecerreyes, E. Unger, A. Abate, M. Stolterfoht, B. Stannowski, R. Schlatmann, et al. *Science* **2023**, *381*, 63.
- [29] J. H. Noh, S. H. Im, J. H. Heo, T. N. Mandal, S. I. Seok, *Nano Lett.* **2013**, *13*, 1764.
- [30] T. J. Jacobsson, J.-P. Correa-Baena, M. Pazoki, M. Saliba, K. Schenk, M. Grätzel, A. Hagfeldt, *Energy Environ. Sci.* **2016**, *9*, 1706.
- [31] Y. Li, B. Shi, Q. Xu, L. Yan, N. Ren, Y. Chen, W. Han, Q. Huang, Y. Zhao, X. Zhang, *Adv. Energy Mater.* **2021**, *11*, 2102046.
- [32] X. Luo, H. Luo, H. Li, R. Xia, X. Zheng, Z. Huang, Z. Liu, H. Gao, X. Zhang, S. Li, Z. Feng, Y. Chen, H. Tan, *Adv. Mater.* **2023**, *35*, 2207883.
- [33] L. Mao, T. Yang, H. Zhang, J. Shi, Y. Hu, P. Zeng, F. Li, J. Gong, X. Fang, Y. Sun, X. Liu, J. Du, A. Han, L. Zhang, W. Liu, F. Meng, X. Cui, Z. Liu, M. Liu, *Adv. Mater.* **2022**, *34*, 2206193.
- [34] X. Y. Chin, D. Turkay, J. A. Steele, S. Tabean, S. Eswara, M. Mensi, P. Fiala, C. M. Wolff, A. Paracchino, K. Artuk, D. Jacobs, Q. Guesnay, F. Sahli, G. Andreatta, M. Boccard, Q. Jeangros, C. Ballif, *Science* **2023**, *381*, 59.
- [35] G. Mahmoudi, V. Stilinović, A. Bauzá, A. Frontera, A. Bartyzel, C. Ruiz-Pérez, A. M. Kirillov, *RSC Adv.* **2016**, *6*, 60385.
- [36] A. Jana, M. Mittal, A. Singla, S. Sapra, *Chem. Commun.* **2017**, *53*, 3046.
- [37] Q. Jiang, Z. Chu, P. Wang, X. Yang, H. Liu, Y. Wang, Z. Yin, J. Wu, X. Zhang, J. You, *Adv. Mater.* **2017**, *29*, 1703852.
- [38] G. Zeng, G. Liu, X. Li, *ACS Sustainable Chem. Eng.* **2023**, *11*, 7664.
- [39] H.-Y. Wang, M.-Y. Hao, J. Han, M. Yu, Y. Qin, P. Zhang, Z.-X. Guo, X.-C. Ai, J.-P. Zhang, *Chem. - Eur. J.* **2017**, *23*, 3986.
- [40] S.-Y. Kim, H. J. Jo, S.-J. Sung, D.-H. Kim, *APL Mater.* **2016**, *4*, 100901.
- [41] M. Sun, C. Liang, H. Zhang, C. Ji, F. Sun, F. You, X. Jing, Z. He, J. Mater. Chem. A **2018**, *6*, 24793.
- [42] J. Mo, C. Zhang, J. Chang, H. Yang, H. Xi, D. Chen, Z. Lin, G. Lu, J. Zhang, Y. Hao, *J. Mater. Chem. A* **2017**, *5*, 13032.
- [43] J. Wu, X. Xu, Y. Zhao, J. Shi, Y. Xu, Y. Luo, D. Li, H. Wu, Q. Meng, *ACS Appl. Mater. Interfaces* **2017**, *9*, 26937.
- [44] O. Er-raji, L. Rustam, B. P. Kore, S. W. Glunz, P. S. C. Schulze, *ACS Appl. Energy Mater.* **2023**, *6*, 6183.
- [45] W. Zhou, Y. Zhao, X. Zhou, R. Fu, Q. Li, Y. Zhao, K. Liu, D. Yu, Q. Zhao, *J. Phys. Chem. Lett.* **2017**, *8*, 4122.
- [46] D. W. deQuilettes, W. Zhang, V. M. Burlakov, D. J. Graham, T. Leijtens, A. Osherov, V. Bulović, H. J. Snaith, D. S. Ginger, S. D. Stranks, *Nat. Commun.* **2016**, *7*, 11683.
- [47] C. Eames, J. M. Frost, P. R. F. Barnes, B. C. O'Regan, A. Walsh, M. S. Islam, *Nat. Commun.* **2015**, *6*, 7497.
- [48] E. Gutierrez-Partida, H. Hempel, S. Caicedo-Dávila, M. Raoufi, F. Peña-Camargo, M. Grischek, R. Gunder, J. Diekmann, P. Caprioglio, K. O. Brinkmann, H. Köbler, S. Albrecht, T. Riedl, A. Abate, D. Abou-Ras, T. Unold, D. Neher, M. Stolterfoht, *ACS Energy Lett.* **2021**, *6*, 1045.
- [49] L. Krückemeier, U. Rau, M. Stolterfoht, T. Kirchartz, *Adv. Energy Mater.* **2020**, *10*, 1902573.
- [50] A. R. b. Mohd Yusoff, M. Vasilopoulou, D. G. Georgiadou, L. C. Palilis, A. Abate, M. K. Nazeeruddin, *Energy Environ. Sci.* **2021**, *14*, 2906.
- [51] M. Stolterfoht, P. Caprioglio, C. M. Wolff, J. A. Márquez, J. Nordmann, S. Zhang, D. Rothhardt, U. Hörmann, Y. Amir, A. Redinger, L. Kegelmann, F. Zu, S. Albrecht, N. Koch, T. Kirchartz, M. Saliba, T. Unold, D. Neher, *Energy Environ. Sci.* **2019**, *12*, 2778.
- [52] M. Stolterfoht, M. Grischek, P. Caprioglio, C. M. Wolff, E. Gutierrez-Partida, F. Peña-Camargo, D. Rothhardt, S. Zhang, M. Raoufi, J. Wolansky, M. Abdi-Jalebi, S. D. Stranks, S. Albrecht, T. Kirchartz, D. Neher, *Adv. Mater.* **2020**, *32*, 2000080.
- [53] P. Fassel, V. Lami, F. J. Berger, L. M. Falk, J. Zaumseil, B. S. Richards, I. A. Howard, Y. Vaynzof, U. W. Paetzold, *Matter* **2021**, *4*, 1391.

- [54] S. Zhang, P. E. Shaw, G. Zhang, H. Jin, M. Tai, H. Lin, P. Meredith, P. L. Burn, D. Neher, M. Stolterfoht, *ACS Appl. Mater. Interfaces* **2020**, *12*, 37647.
- [55] S. Gharibzadeh, P. Fassl, I. M. Hossain, P. Rohrbeck, M. Frericks, M. Schmidt, T. Duong, M. R. Khan, T. Abzieher, A. N. B., F. Schackmar, O. Almora, T. Feeney, R. Singh, D. Fuchs, U. Lemmer, J. P. Hofmann, S. A. L. Weber, U. W. Paetzold, *Energy Environ. Sci.* **2021**, *14*, 5875.
- [56] Y. Shi, E. Rojas-Gatjens, J. Wang, J. Pothoof, R. Giridharagopal, K. Ho, F. Jiang, M. Taddei, Z. Yang, E. M. Sanehira, M. D. Irwin, C. Silva-Acuña, D. S. Ginger, *ACS Energy Lett.* **2022**, *7*, 4081.
- [57] J. Warby, F. Zu, S. Zeiske, E. Gutierrez-Partida, L. Frohloff, S. Kahmann, K. Frohna, E. Mosconi, E. Radicchi, F. Lang, S. Shah, F. Peña-Camargo, H. Hempel, T. Unold, N. Koch, A. Armin, F. D. Angelis, S. D. Stranks, D. Neher, M. Stolterfoht, *Adv. Energy Mater.* **2022**, *12*, 2103567.
- [58] F. Peña-Camargo, P. Caprioglio, F. Zu, E. Gutierrez-Partida, C. M. Wolff, K. Brinkmann, S. Albrecht, T. Riedl, N. Koch, D. Neher, M. Stolterfoht, *ACS Energy Lett.* **2020**, *5*, 2728.
- [59] C. M. Wolff, S. A. Bourelle, L. Q. Phuong, J. Kurpiers, S. Feldmann, P. Caprioglio, J. A. Marquez, J. Wolansky, T. Unold, M. Stolterfoht, S. Shoaee, F. Deschler, D. Neher, *Adv. Energy Mater.* **2021**, *11*, 2101823.
- [60] N. E. Courtier, *Phys. Rev. Appl.* **2020**, *14*, 024031.
- [61] M. A. Green, A. W. Y. Ho-Baillie, *ACS Energy Lett.* **2019**, *4*, 1639.
- [62] W. Yang, H. Long, X. Sha, J. Sun, Y. Zhao, C. Guo, X. Peng, C. Shou, X. Yang, J. Sheng, Z. Yang, B. Yan, J. Ye, *Adv. Funct. Mater.* **2021**, *32*, 2110698.
- [63] N. Li, Y. Luo, Z. Chen, X. Niu, X. Zhang, J. Lu, R. Kumar, J. Jiang, H. Liu, X. Guo, B. Lai, G. Brocks, Q. Chen, S. Tao, D. P. Fenning, H. Zhou, *Joule* **2020**, *4*, 1743.
- [64] M. Yavari, X. Liu, T. Webb, K. D. G. I. Jayawardena, Y. Xiang, S. Kern, S. Hinder, T. J. Macdonald, S. R. P. Silva, S. J. Sweeney, W. Zhang, *J. Mater. Chem. C* **2021**, *9*, 4367.
- [65] J. Wang, L. Yuan, H. Luo, C. Duan, B. Zhou, Q. Wen, K. Yan, *Chem. Eng. J.* **2022**, *446*, 136968.
- [66] A. Farag, R. Schmager, P. Fassl, P. Noack, B. Wattenberg, T. Dippell, U. W. Paetzold, *ACS Appl. Energy Mater.* **2022**, *5*, 6700.
- [67] D. Menzel, A. Al-Ashouri, A. Tejada, I. Levine, J. A. Guerra, B. Rech, S. Albrecht, L. Korte, *Adv. Energy Mater.* **2022**, *12*, 2201109.
- [68] C. Wang, C. Zhang, S. Wang, G. Liu, H. Xia, S. Tong, J. He, D. Niu, C. Zhou, K. Ding, Y. Gao, J. Yang, *Sol. RRL* **2018**, *2*, 1700209.
- [69] G. Zhou, J. Wu, Y. Zhao, Y. Li, J. Shi, Y. Li, H. Wu, D. Li, Y. Luo, Q. Meng, *ACS Appl. Mater. Interfaces* **2018**, *10*, 9503.
- [70] M. Saliba, T. Matsui, J.-Y. Seo, K. Domanski, J.-P. Correa-Baena, M. K. Nazeeruddin, S. M. Zakeeruddin, W. Tress, A. Abate, A. Hagfeldt, M. Grätzel, *Energy Environ. Sci.* **2016**, *9*, 1989.
- [71] N. Zhou, Y. Shen, Y. Zhang, Z. Xu, G. Zheng, L. Li, Q. Chen, H. Zhou, *Small* **2017**, *13*, 1700484.
- [72] T. Liu, H. Lai, X. Wan, X. Zhang, Y. Liu, Y. Chen, *Chem. Mater.* **2018**, *30*, 5264.
- [73] B. Li, W. Zhang, *Commun. Mater.* **2022**, *3*, 65.
- [74] M. Kim, G.-H. Kim, T. K. Lee, I. W. Choi, H. W. Choi, Y. Jo, Y. J. Yoon, J. W. Kim, J. Lee, D. Huh, H. Lee, S. K. Kwak, J. Y. Kim, D. S. Kim, *Joule* **2019**, *3*, 2179.
- [75] B. L. Welch, *Biometrika* **1947**, *34*, 28.
- [76] G. D. Ruxton, *Behav. Ecol.* **2006**, *17*, 688.
- [77] B. Derrick, P. White, *Quant. Meth. Psych.* **2016**, *12*, 30.
- [78] Dotmatics, Graphpad: T test calculator, <https://www.graphpad.com/quickcalcs/ttest1/?format=C>, (accessed: June, 2023).